

## Characterization of front contact degradation in monocrystalline and multicrystalline silicon photovoltaic modules following damp heat exposure

Nafis Iqbal <sup>a,b,\*</sup>, Dylan J. Colvin <sup>a,b,c</sup>, Eric J. Schneller <sup>a,b,c</sup>, Tamil S. Sakthivel <sup>a,d</sup>, Roger Ristau <sup>e</sup>, Bryan D. Huey <sup>e</sup>, Ben X.J. Yu <sup>f</sup>, Jean-Nicolas Jaubert <sup>f</sup>, Alan J. Curran <sup>g,h</sup>, Menghong Wang <sup>g</sup>, Sudipta Seal <sup>a,d</sup>, Roger H. French <sup>g,h,i</sup>, Kristopher O. Davis <sup>a,b,c,j,\*</sup>

<sup>a</sup> Department of Materials Science and Engineering, University of Central Florida, Orlando, FL, USA

<sup>b</sup> Resilient, Intelligent and Sustainable Energy Systems (RISES) Cluster, University of Central Florida, Orlando, FL, USA

<sup>c</sup> FSEC Energy Research Center, Cocoa, FL, USA

<sup>d</sup> Advanced Materials Processing and Analysis Center, NanoScience and Technology Center, University of Central Florida, Orlando, FL, USA

<sup>e</sup> Institute of Materials Science, University of Connecticut, Storrs, CT, USA

<sup>f</sup> Canadian Solar, Inc., Guelph, Ontario, Canada

<sup>g</sup> SDLE Research Center, Case Western Reserve University, Cleveland, OH, USA

<sup>h</sup> Department of Materials Science and Engineering, Case Western Reserve University, Cleveland, OH, USA

<sup>i</sup> Department of Macromolecular Science and Engineering, Case Western Reserve University, Cleveland, OH, USA

<sup>j</sup> CREOL, the College of Optics and Photonics, University of Central Florida, Orlando, FL, USA

### ARTICLE INFO

#### Keywords:

Crystalline silicon  
Photovoltaics  
Solar cells  
PERC  
Contact degradation  
Metallization corrosion

### ABSTRACT

Reliability and durability tests play a key role in the photovoltaic (PV) industry by minimizing potential failure risks for both existing and new cell and module technologies. In this work, a detailed study of contact degradation in monocrystalline and multicrystalline PV modules is performed. The modules are subjected to a sequence of damp heat (DH) exposures followed by electrical characterization after each step. Electroluminescence (EL) imaging shows different darkening patterns for monocrystalline modules compared to multicrystalline modules; the former shows darkening near the busbars and the latter shows it across virtually the entire cell surface. The primary loss mechanism is confirmed to be resistive after comparing the current-voltage (*I*-*V*) characteristics at each DH exposure step. Representative samples have been cored out from both the degraded modules and controls for materials characterization to gain further insights into the degradation mechanism. Top-down and cross-sectional scanning electron microscopy (SEM), energy dispersive spectroscopy (EDS), and top-down high-resolution X-ray photoelectron spectroscopy (XPS) analysis performed on the cored samples confirm the degradation is due to metallization corrosion. Our study suggests that the difference in the darkening pattern can most likely be attributed to the different silver paste composition used for contacting each cell technology, particularly the composition of the glass frit.

### 1. Introduction

Silicon photovoltaic (PV) modules are impressively reliable [1]. 30-year warranties are becoming more commonplace as a result of the decades of engineering and scientific research invested in the materials and processes used to continually improve PV devices [2]. In fact, the excellent reliability and low power loss ( $\leq 1\%$  per year) [3,4] help make solar energy highly competitive with other energy sources by lowering

the PV leveled cost-of-energy (LCOE) [5]. The innovations required to make PV modules reliable and durable come from studying degradation. A detailed understanding of how module performance degrades over time is essential to engineering better modules and processes. One of the techniques to qualify modules for mass production is accelerated aging. Accelerated aging tests induce forms of degradation or failure modes commonly observed in field-installed modules (e.g., encapsulant discoloration, metallization corrosion, interconnect breakage) [4,6–10].

\* Corresponding author. Department of Materials Science and Engineering, University of Central Florida, Orlando, FL, USA.

E-mail addresses: [nafisiqbalknights.ucf.edu](mailto:nafisiqbalknights.ucf.edu) (N. Iqbal), [kristopher.davis@ucf.edu](mailto:kristopher.davis@ucf.edu) (K.O. Davis).

**Table 1**

Silver paste composition (in wt.%) used for monocrystalline PERC and multicrystalline Al-BSF cells obtained with XRF before firing.

Monocrystalline PERC		Multicrystalline Al-BSF	
Element	Wt.%	Element	Wt.%
Ag	96.24	Ag	95.98
PbO	0.79	PbO	0.098
ZnO	0.078	ZnO	0.197
SiO <sub>2</sub>	0.58	SiO <sub>2</sub>	0.987
Bi <sub>2</sub> O <sub>3</sub>	0.422	Bi <sub>2</sub> O <sub>3</sub>	0.246
CuO	0.018	CuO	0.016
Fe <sub>2</sub> O <sub>3</sub>	0.027	Fe <sub>2</sub> O <sub>3</sub>	0.026
MoO <sub>3</sub>	0.007	MoO <sub>3</sub>	0.146
In <sub>2</sub> O <sub>3</sub>	0.352	In <sub>2</sub> O <sub>3</sub>	0.35
TeO <sub>2</sub>	1.21	TeO <sub>2</sub>	1.4
WO <sub>3</sub>	0.073	TiO <sub>2</sub>	0.03
SeO <sub>2</sub>	0.0684	Pd	0.22
SO <sub>3</sub>	0.017	MgO	0.144
P <sub>2</sub> O <sub>5</sub>	0.013	B <sub>2</sub> O <sub>3</sub>	0.16
Na <sub>2</sub> O	0.043	–	–
CaO	0.0616	–	–

These tests can turn years into days by inducing extreme doses of relevant environmental stressors, such as UV light, thermal fluctuations, wind or snow loading, and humidity.

**Damp-heat (DH)** testing is one of the most common accelerated aging tests applied to PV modules [11] for qualification. DH testing typically consists of leaving a module in a chamber that is 85 °C and at 85% relative humidity for a number of hours. One of the most prominently noticeable phenomena due to DH testing is the darkening of the cells observed in electroluminescence (EL) imaging. This failure mechanism related to DH-induced degradation has been attributed to the metallization corrosion by previous findings [11,12]. Corrosion of the metallization and interconnects is commonly observed in field exposed modules [3,4,9,10]. Ethylene-vinyl acetate (EVA), a common encapsulant for PV modules, decomposes to produce acetic acid when exposed to ultraviolet (UV) radiation and is exacerbated by elevated temperature and the presence of moisture. Notably, additives within the EVA can either enhance or reduce acetic acid formation (more precisely, acetic acid and polyene formation via side group deacetylation is influenced by additives; see Ref. [13] for a deeper discussion). This tends to lower the pH and accelerates the rate of corrosion [14]. Acetic acid attacks the thin glass layer found between the silver (Ag) metallization and silicon (Si) emitter resulting in increased series resistances [11]. It has been found that acetic acid reacts with the lead-oxide (PbO) in the glass layer to form lead acetate. The lead (Pb) is then re-deposited away from the glass layer. This is a repetitive cyclical process that accelerates the dissolution of the glass layer, forming a gap between the Ag contact and the Si emitter [15]. A recent study confirmed this phenomenon and has also shown that there is a Pb alternation layer formed in the metal-Si interface that inhibits carrier transport [16].

In this work, we investigate the front contact degradation of multicrystalline and monocrystalline PV modules exposed to DH. Current-voltage (*I*-*V*) measurements and EL imaging were performed at each step of DH to analyze the electrical performance degradation. Furthermore, photoluminescence (PL) imaging, external quantum efficiency (EQE), and reflectance (R) analyses were performed to investigate the optical losses. Representative samples were cored out from the modules and further materials characterization were performed. The microscopic and elemental analysis of the degraded regions were compared with non-degraded control samples to investigate the root cause of performance degradation.

## 2. Experiment

### 2.1. Module specification, characterization and sample coring

Two monocrystalline Si passivated emitter and rear cell (PERC) modules and two multicrystalline Si aluminium back surface field (Al-BSF) modules were selected for this experiment. Both module types contain 144 five-busbar half cells (156.75 × 78.38 mm) in a (2 × (12 × 6)) cell arrangement. The silver paste compositions used to contact the two different cell technologies are different, primarily due to the requirement of various oxides to adhere to monocrystalline and multicrystalline cells. Table 1 shows the silver paste elemental composition values which was obtained by the cell manufacturer before firing by X-ray fluorescence (XRF) (variability ≈ ±5%). The major compositional differences between the two pastes can be seen for PbO (0.79 wt.% for monocrystalline and 0.098 wt.% for multicrystalline), ZnO (0.078 wt.% for monocrystalline and 0.197 wt.% for multicrystalline) and SiO<sub>2</sub> (0.58 wt.% for monocrystalline and 0.987 wt.% for multicrystalline). These differences in paste compositions between suppliers are due to optimizing pastes for better adhesion and contact formation for different doping layers and Si surface morphologies. The optimized peak firing temperature for monocrystalline PERC cells were 765 ± 10 °C and multicrystalline Al-BSF cells were 790 ± 10 °C. The cells were co-fired in an infrared (IR) heated belt furnace. All the modules have clear EVA for front encapsulation. For the rear side, monocrystalline PERC modules have white EVA and the multicrystalline Al-BSF modules have the clear EVA. ZTT-KPO backsheets is used for monocrystalline modules with a water vapor transmission rate (WVTR) of 0.9–1.1 g/m<sup>2</sup> per day. For multicrystalline, the backsheets is Cybrid KPF with WVTR of ≈1.7 g/m<sup>2</sup> per day.

One of each type of modules underwent 3200 h of damp heat exposure at 85 °C and 85% relative humidity according to IEC 61215-2: 2016 international standard [17]. Each module was characterized with illuminated and dark *I*-*V* measurements. Illuminated *I*-*V* was performed using a solar simulator at an accredited module characterization facility. *I*-*V* data were obtained at each step of DH exposure (0, 1000, 2000, 2400, 2800, and 3200 h). Series resistance values were calculated using the method described in Ref. [18]. EL images were taken using a modified digital single-lens reflex (DSLR) camera.

The EL images were used to select regions of interest located towards the edge of the modules for extracting circular sections of cells in a process similar to “partial coring” used in Refs. [19,20]. To maintain consistency, cored samples from identical locations (mid-bottom section of each of the modules) were selected for further materials characterization. Our coring process consisted of fastening a module to a drill press equipped with a mill bit of 0.5 inches in diameter. An adhesive was used to connect a custom machined metal post to the back of the sample. Once fully dried, heat was applied to the front glass, and the sample was gently twisted until it was released from the module. Acetone and manual diamond wire sawing were used to remove the cored sections from the metal post for preparing samples for further materials characterization. As used in Refs. [19,20], a longer acetone soak removes the need for wire sawing and is recommended. Our coring process along with EL images helped us to keep track of the position and condition (degradation) of each of the samples for consistency during the analysis.

### 2.2. Cell and cored sample characterization

Prior to coring, EQE and R measurements were performed on several cells within the module using a FlashQE system by Tau Science Corporation. This tool is an LED-based QE measurement system with a spot size of 4 mm. The system is equipped with an array of 41 independent LEDs, representing 41 different wavelengths. It is also equipped with an integrating sphere used for measuring reflectance at each location [21–23]. It uses unique modulation frequencies for the LEDs in order to perform full spectrum measurements which take about 1 s. Openings

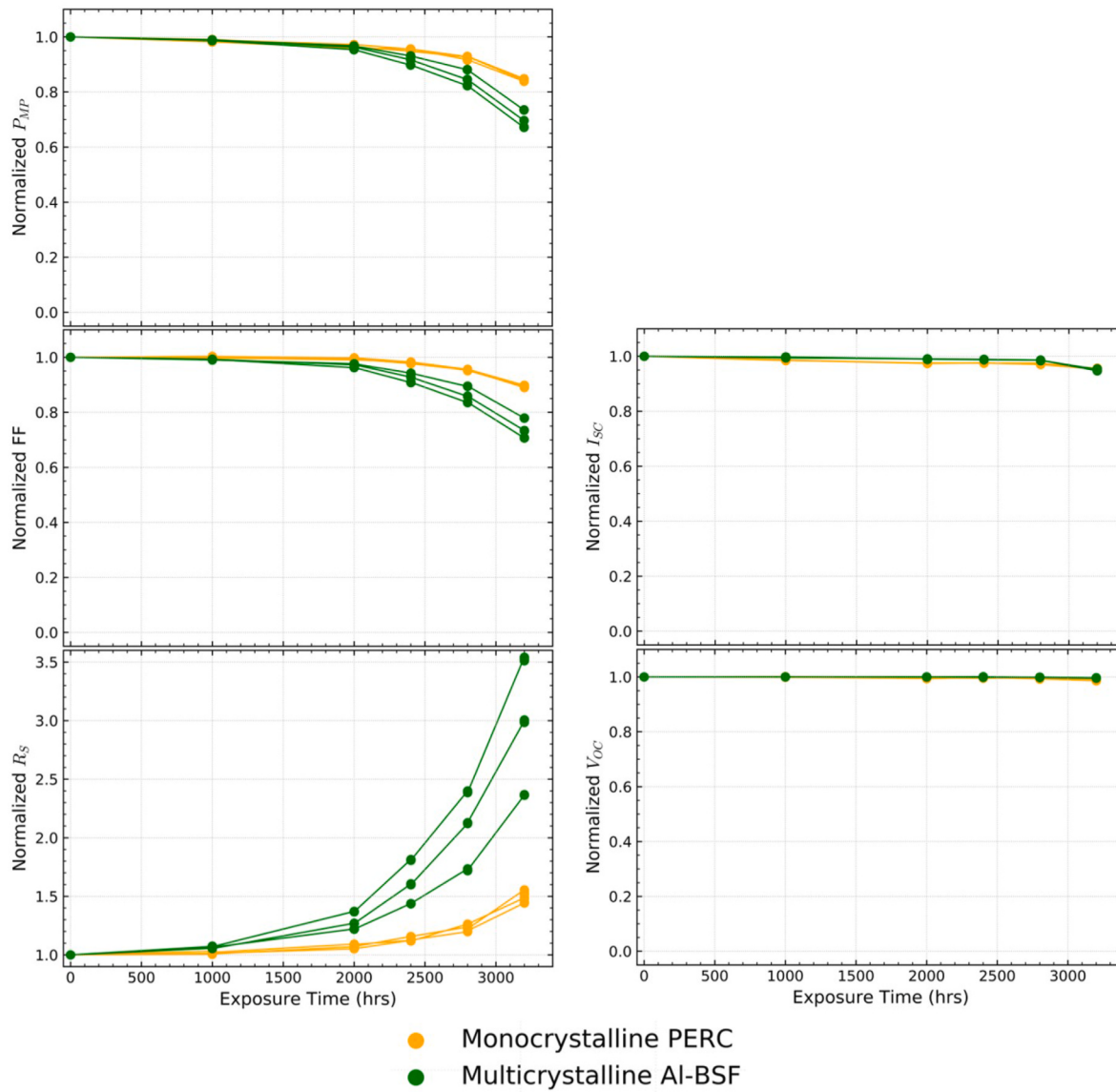


**Fig. 1.** *I-V* performance comparison of monocrystalline PERC and multicrystalline Al-BSF modules after each step of damp heat exposure.

were made on the rear side of the module for electrical connection. EQE and reflectance data for individual cells within the modules were recorded.

A BT Imaging LIS-R1 PL system was used in this experiment to obtain open-circuit PL images of the cored samples. The system contains an 808 nm wavelength laser as the excitation source. The emitted PL signal was captured by a 1-megapixel silicon charge-coupled device (CCD) camera with a 920 nm long-pass filter. PL images were recorded at 1 and 0.1 suns, respectively. In this experiment, photon flux values of  $3.085 \times 10^{17} \text{ cm}^{-2}\text{s}^{-1}$  and  $3 \times 10^{16} \text{ cm}^{-2}\text{s}^{-1}$  were assumed to be 1 sun and 0.1 suns respectively, which were determined by calibrating the photon flux values towards matching the short-circuit current density ( $J_{SC}$ ) of a reference solar cell with known EQE data [21,24].

Top-down scanning electron microscopy (SEM) and energy dispersive spectroscopy (EDS) analysis on the Ag metal contacts were performed using a ZEISS ULTRA 55 SEM. Identical regions on the Ag metal contacts located between 1 mm and 4 mm from the busbar were selected both for control and degraded samples. An acceleration voltage of 2 kV, a working distance of 5 mm, and a secondary electron (SE) detector were used to capture the images. EDS analysis was performed using an acceleration voltage of 30 kV, a working distance of 13 mm, and the EDS

detector. ZEISS SmartSEM software was used to collect and analyze the SEM images and EDS data. For the cross-sectional images, a FEI Helios 460F1 system was used to perform focused ion beam (FIB) sectioning, SEM imaging and EDS analysis. An acceleration voltage of 5 kV, a working distance of 4 mm, an angle of 52° and a secondary electron (SE) detector were used for imaging and elemental analysis. Furthermore, top-down SEM and EDS analysis on the glass layer was also performed after removing bulk Ag. The analysis locations were similar to the top-down SEM and EDS. The samples were dipped in 70% nitric acid ( $\text{HNO}_3$ ) for 90 min at 45 °C to remove the bulk Ag and access the underlying glass layer [25,26]. It is to be noted that this process etches away the bulk Ag, but the underlying glass layer remains intact. To remove the glass layer, further etching is needed with a different chemical solution (e.g., hydrofluoric acid) [25,26].

X-ray photoelectron spectroscopy (XPS) analysis was performed on top of the Ag fingers and on the glass layer (after bulk Ag removal) using a Thermo Scientific ESCALAB-250Xi spectrometer in an ultra-high vacuum (UHV) chamber (below  $7 \times 10^{-9}$  mbar). High-resolution XPS analysis combined with SEM and EDS can be a powerful tool to study the reliability and degradation of materials. With the help of EL images to locate the dark areas, we selected similar regions on the finger that are

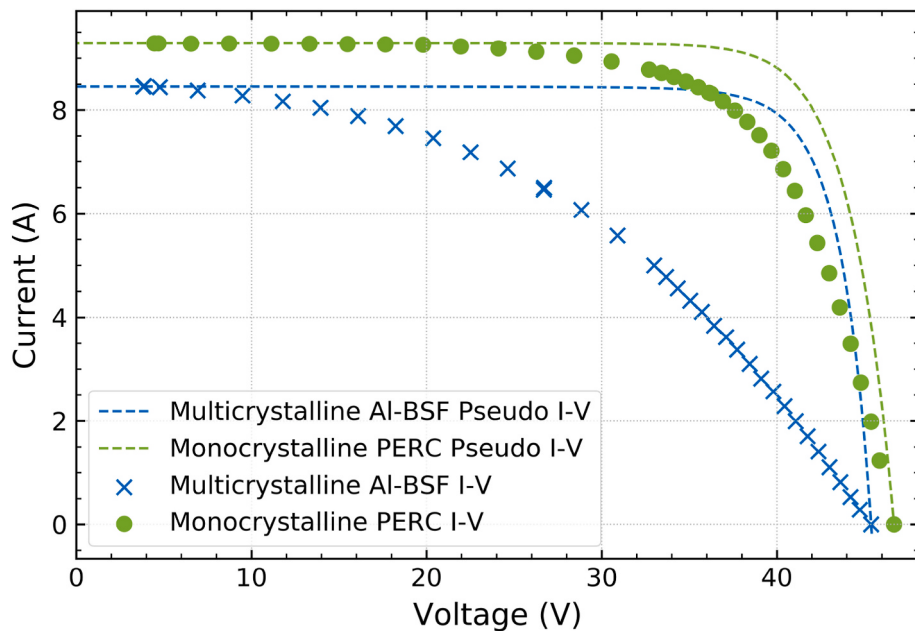


Fig. 2. Representative  $I$ - $V$  curves with pseudo- $I$ - $V$ , obtained from Suns- $V_{OC}$ , for a module after 3200 h DH exposure. A Sinton FMT-350 was used to obtain these data.

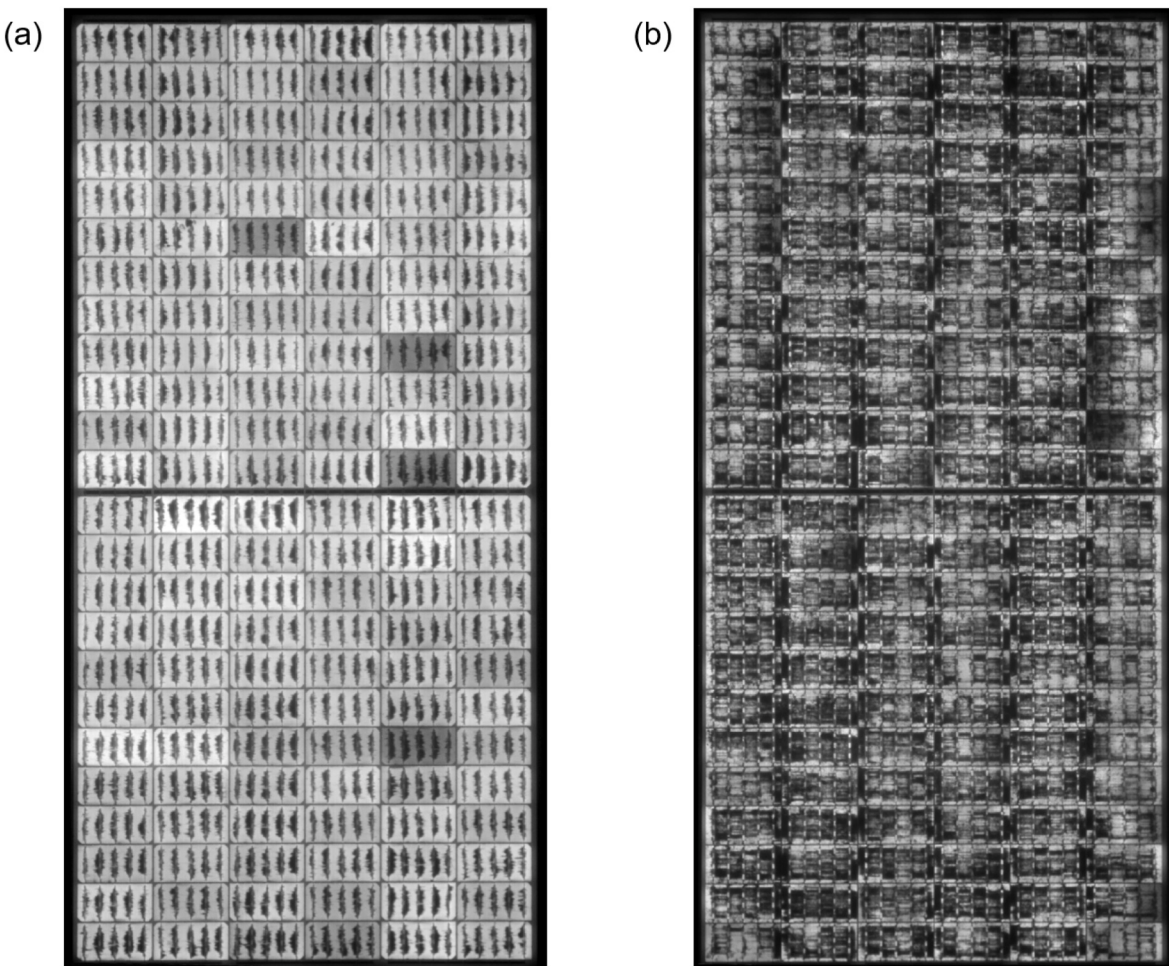
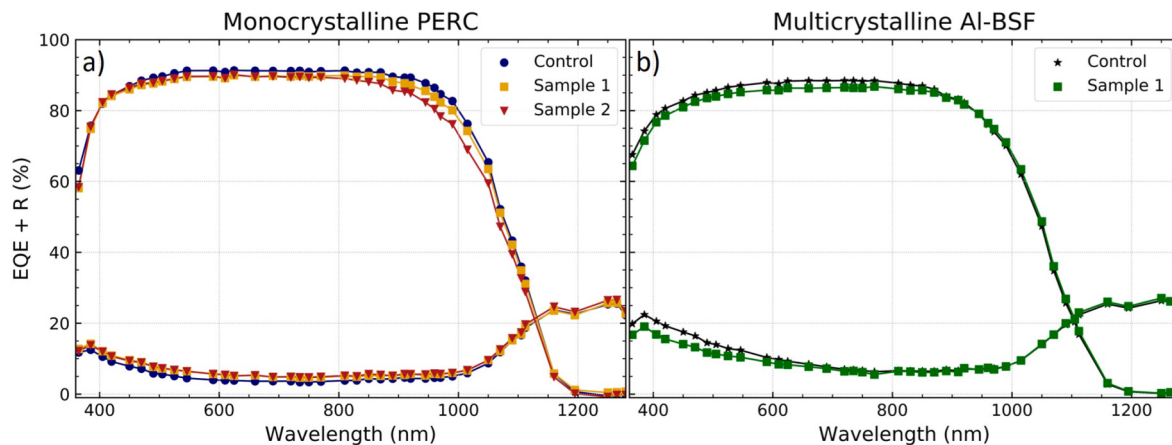


Fig. 3. EL images of (a) monocrystalline and (b) multicrystalline module after 3200 h of damp heat testing.



**Fig. 4.** Comparison of EQE performance and reflectance ( $R$ ) for a) monocrystalline PERC and b) multicrystalline Al-BSF modules after 3200 h of damp heat exposure.

between 1 mm and 4 mm from the busbar both for control and degraded samples. An  $\text{Al-K}_\alpha$  monochromatic radiation source (binding energy 1486 eV) was used, operating at a power of 300 W (15 kV, 20 mA). The spot size of the X-ray was 200  $\mu\text{m}$  and C 1s peak at 284.8 eV was used as a base for calibration within an experimental error of  $\pm 0.2$  eV. Depth profile was applied up to 20 levels using an Ar gas cluster ion beam (Ar GCIB). Approximately 1.5 nm thickness was removed on each level resulting in an overall  $\approx 30$  nm removal of material. Both the survey spectrum and high-resolution elemental spectrum were collected before and after depth profile. XPS imaging was recorded with the full range of the spectrum after 20 level of depth profiling. 650  $\mu\text{m}$  spot size with lower pass energy (20 eV) was utilized for better resolution imaging. A Thermo Scientific Avantage Data System software was used to record and analyze (processing, deconvolution, peak fitting and atomic % profile mapping) the data. The uncertainty in the peak fitting spectra is in the order of  $\pm 0.4$  eV.

### 3. Results and discussion

#### 3.1. Decoupling performance losses

The primary  $I$ - $V$  data obtained at each step of DH exposure reveal that the open-circuit voltage ( $V_{OC}$ ) drops by approximately 0.3–1.4% (system variability  $\pm 1.8\%$ ), while the short-circuit current ( $I_{SC}$ ) drops by approximately  $5 \pm 0.7\%$  for the monocrystalline PERC and multicrystalline Al-BSF modules (Fig. 1). The  $I_{SC}$  of the PERC module steadily decreases up to 2800 h exposure, while the Al-BSF modules'  $I_{SC}$  remains static. At 3200 h, the  $I_{SC}$  of each module drops by approximately 5% absolute from the baseline. The degradation in maximum power ( $P_{MP}$ ), series resistance ( $R_S$ ), and fill factor (FF) reveals that the primary loss mechanism is resistive. Comparing  $I$ - $V$  with Suns- $V_{OC}$  also confirms significant resistive loss (see Fig. 2). It has been shown that Suns- $V_{OC}$  can be used to give an equivalent  $I$ - $V$  curve for a device as if it had no  $R_S$  [27]. As seen in Fig. 3, there is a darkening of the cells observed in the EL images which shows greater degradation for the multicrystalline versus the monocrystalline modules. In both cases, darkening begins at the busbars (see supplementary information S1) and extends from there. However, multicrystalline modules also show darkening at the short

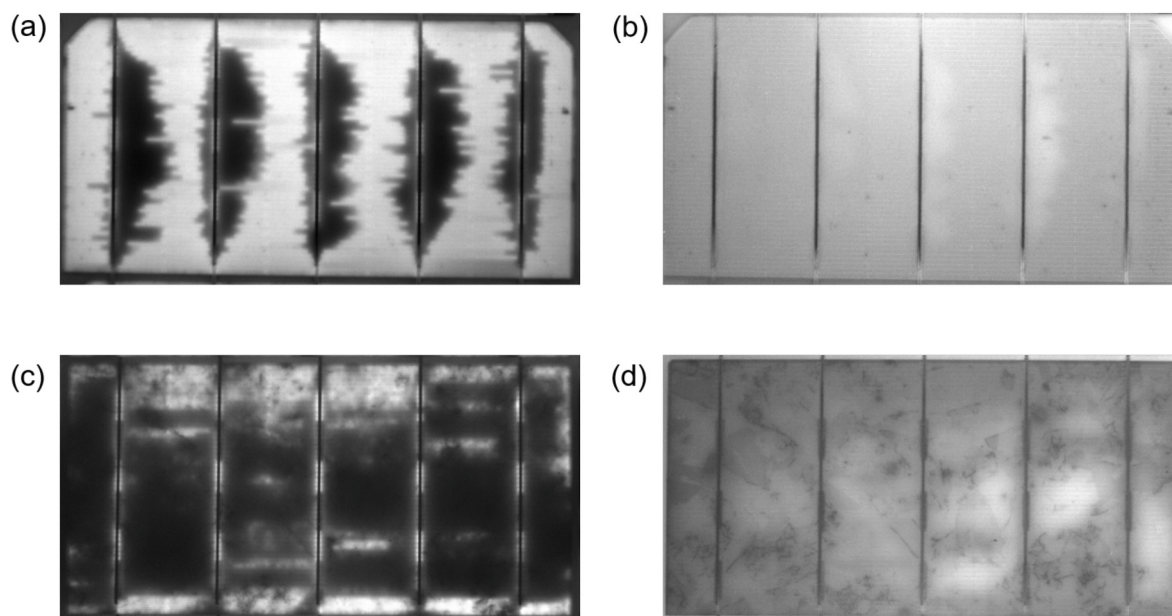


**Fig. 5.** Comparison of cell level EL (a,c) and PL (b,d) images for single half-cell within monocrystalline PERC (top row) and multicrystalline Al-BSF (bottom row) modules after 3200 h of damp heat exposure.

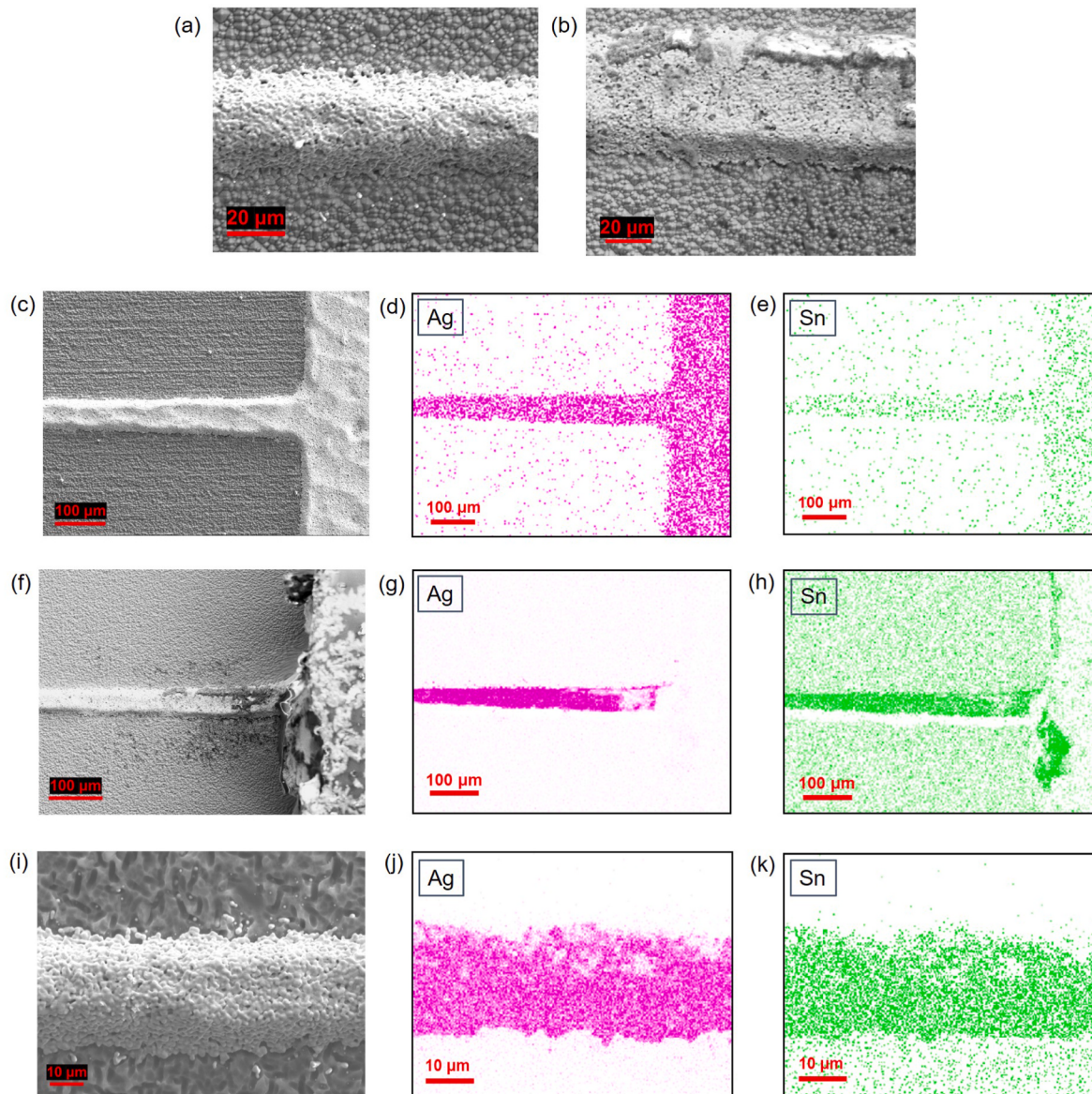


**Fig. 6.** Comparison between (a) control and (b) degraded monocrystalline gridline (top row). Top-down SEM image (c,f,i) and Ag EDS map (d,g,j), Sn EDS map (e,h,k) comparison for gridlines from control monocrystalline PERC (second row), degraded monocrystalline PERC (third row) and degraded multicrystalline Al-BSF (bottom row) samples.

edges of the cells after 3200 h of DH exposure, resulting in darkening patterns across the entire cell surface.

In order to examine optical losses, EQE and reflectance (R) data were obtained for cells within both modules, as shown in Fig. 4. EQE results show that for monocrystalline PERC, the largest differences (2.25–3.20% absolute) occur between 810–1110 nm range between the control and sample 2. The lower EQE response in sample 2 is evidently recombination based, since the reflectance is negligibly higher than the control module and the EL of this cell shows uniform darkening. EQE analysis shows that the loss occurs in the base region of the cell. For multicrystalline Al-BSF, the largest differences (1.94–3.18% absolute) between the control and the degraded is shown within the 365–750 nm range. The increase in reflectance from 365 to 650 nm shows that there is optical loss in the near UV and mid-visible range.

The EQE and R data were further analyzed using the method described in Ref. [21]. The results suggest that there are minor optical and recombination losses for multicrystalline Al-BSF and greater, albeit still minor, recombination losses for monocrystalline PERC. A detailed comparison of the cell level EL and PL images, shown in Fig. 5, provide

further evidence that resistive effects primarily are reducing performance. EL darkening shows severe contact degradation for both sample technologies while PL shows no extraordinary dark regions. Interestingly, for the multicrystalline Al-BSF modules, there is cell darkening both from the busbar and at the short edges after 3200 h of DH exposure, resulting in the contact corrosion pathway being different from that of the monocrystalline PERC modules.

### 3.2. Degradation mechanism

To investigate the root cause for the different darkening pathways for monocrystalline and multicrystalline modules, top-down and cross-sectional SEM imaging and EDS mapping were performed on the cored samples. Fig. 6 shows top-down SEM and EDS analyses performed on the gridlines of control monocrystalline PERC, degraded monocrystalline PERC and multicrystalline Al-BSF samples. Signs of delamination (between bulk Ag and interfacial glass layer) were observed near the edges of fingers for the degraded monocrystalline sample after a visual inspection, which is not present in the control sample (Fig. 6(a)

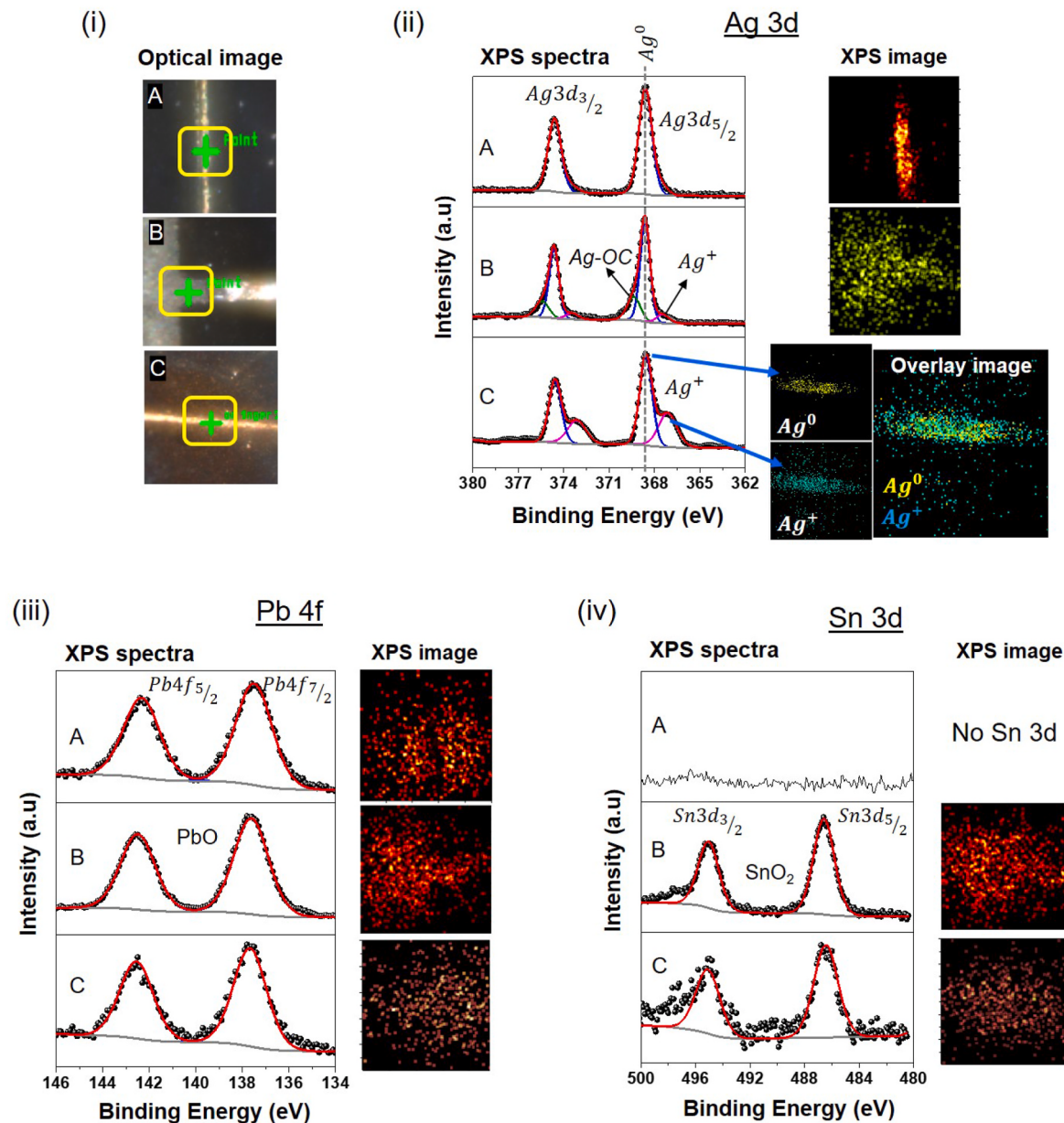


**Fig. 7.** Comparison of the high-resolution XPS spectral lines and corresponding XPS images/mapping obtained at gridlines for (A) control monocrystalline PERC, (B) degraded monocrystalline PERC and (C) degraded multicrystalline Al-BSF samples. (i) Optical image shows the point where the XPS spectral lines and images are recorded on all three samples (Green Cross is the X-ray focus point and yellow square is XPS image projection). (ii) XPS spectral lines of Ag 3d and corresponding XPS image/mapping of control and both degraded samples. The degraded multicrystalline Al-BSF sample clearly indicates the higher oxidation of Ag ( $\text{Ag}^+$ ) compared to the PERC sample. Atomic % profile of Ag and  $\text{Ag}^+$  was generated from XPS imaging and corresponding overlay image show the locations of Ag and  $\text{Ag}^+$ . (iii) Pb 4f and (iv) Sn 3d XPS envelopes along with XPS images. Interestingly, Sn was not identified on the surface of control sample. (For interpretation of the references to color in this figure legend, the reader is referred to the Web version of this article.)

and b)). From the EDS mapping, it is evident that there is Sn (Fig. 6(h,k)) present on the surface of the gridlines for both the degraded samples alongside Ag (Fig. 6(g,j)). However, this is not the case for the control monocrystalline sample which barely has any Sn present (Fig. 6(e)).

XPS analysis performed on the Ag metal fingers is shown in Fig. 7. Fig. 7(i) shows the optical images with the location of the analysis. Here, the green cross is the X-ray focus point and the yellow square is the XPS image projection. Fig. 7(ii) shows the high-resolution Ag 3d XPS spectra for each of the samples after the final step of depth profile. The deconvolution of the peaks suggest that Ag is oxidized for the degraded samples [28,29]. It is also noticeable that multicrystalline samples have greater oxidation of Ag compared to monocrystalline samples. The control sample seems to have no oxidation, as expected. We also

recorded XPS images of the full spectrum for each sample. The control sample clearly shows the presence of metallic Ag on the surface. The highly oxidized multicrystalline sample shows the two deconvoluted peaks for Ag (368.6 eV) and  $\text{Ag}^+$  (367.13 eV). In addition, the degraded PERC sample shows the additional peak of  $\approx 369$  eV belonging to Ag-OC bonding, which is attributed to the oxidized Ag surface bonded with C-O species. Atomic % profile of the Ag 3d images was extracted and the location of Ag and  $\text{Ag}^+$  identified in the degraded Al-BSF sample. The overlay mapping of Ag indicates that both metallic and oxidized Ag is present on the gridline. This confirms that the gridline is corroding for both technologies, as previously observed by other studies [30]. In other words, the oxidation of Ag increases the finger conductor resistance. However, this is not the major factor causing an increase in the series

**Table 2**

Atomic % quantification of XPS survey spectrum for control, degraded monocrystalline PERC and multicrystalline Al-BSF samples after depth profile.

Element	Control	Mono PERC	Multi Al-BSF
	Atomic %	Atomic %	Atomic %
C 1s	13.09	21.6	21.98
Si 2p	31.69	8.71	24.69
N 1s	18.54	25.9	20.29
O 1s	34.12	34.26	29.61
Ag 3d	1.99	2.78	2.80
Sn 3p	–	2.76	0.41
Pb 4f	0.56	3.99	0.22

resistance. If it were, the pattern of the EL image would actually be brighter near the busbars and gradually become darker along the direction of the finger reaching a minimum near the midpoint between

busbars [31]. The influence of WVTR of the backsheets on corrosion rate was also considered; however, the difference between the two WVTRs is small and EL images obtained at each step shows that corrosion starting from the busbar does not begin until 2000 h exposure for monocrystalline and multicrystalline modules. If the difference in WVTRs had a significant influence on DH degradation rate, the multicrystalline modules, with high WVTR backsheets, would have begun darkening earlier than the monocrystalline samples.

Fig. 7(iii) shows the high-resolution XPS spectra and imaging for Pb 4f which suggests the presence of PbO on the surface of all the samples. Quantification of the spectrum (Table 2) reveals a higher amount of Pb for the degraded monocrystalline PERC samples compared to control and multicrystalline Al-BSF samples. Fig. 7(iv) shows the XPS spectral line of Sn 3d and XPS imaging. These results indicate that there is a skin layer of SnO<sub>2</sub> on the surface of the gridlines. Quantification of the survey spectrum suggests there is higher amount of Sn for monocrystalline

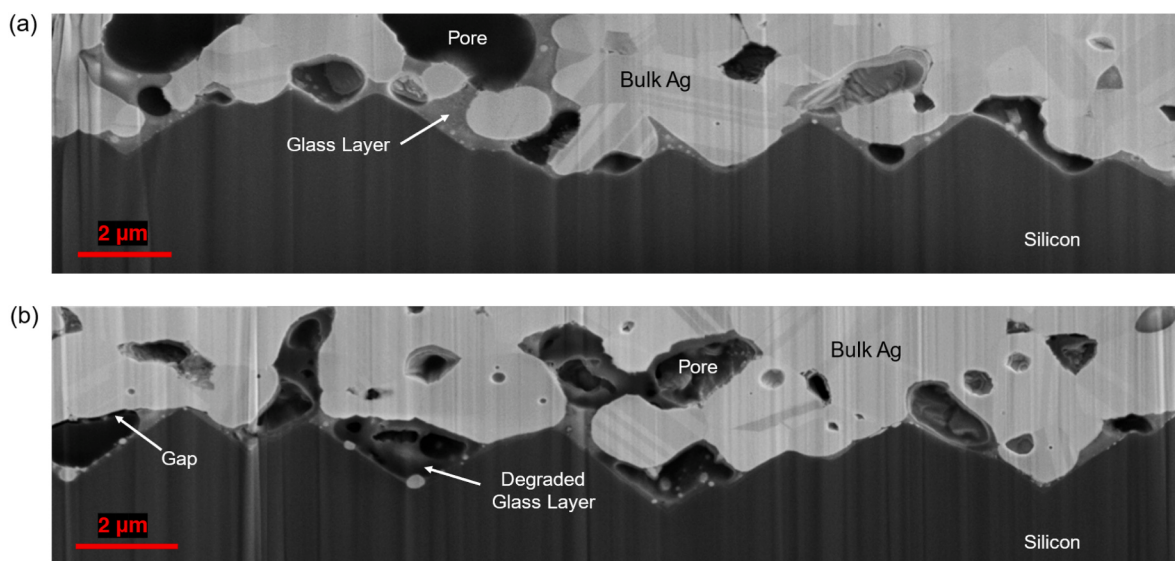


Fig. 8. High resolution cross-sectional SEM images along the metal-Si interface of (a) control and (b) degraded monocrystalline samples.

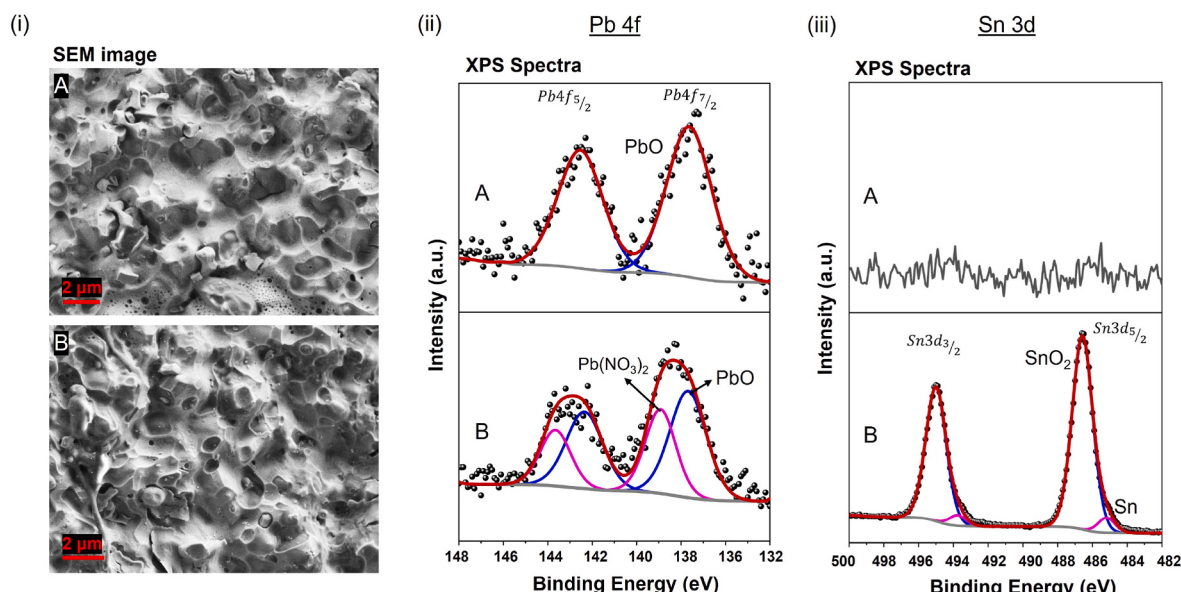


Fig. 9. Comparison of the top-down SEM images and high-resolution XPS spectral lines of the glass layer for the (A) control monocrystalline PERC and (B) degraded monocrystalline PERC samples. (i) SEM images of the control and degraded samples. Visually there seems to be no significant difference. XPS analysis was performed at these locations. (ii) Pb 4f and (iii) Sn 3d XPS spectral lines of the control and degraded samples. Sn was not identified on the control sample.

**Table 3**

Atomic % quantification of the XPS survey spectrum on the glass layer of the control and degraded monocrystalline PERC samples.

Element	Control Mono PERC	Degraded Mono PERC
	Atomic %	Atomic %
C 1s	5.82	6.65
Si 2p	3.62	4.83
O 1s	73.33	67.42
N 1s	3.76	3.21
Ag 3d	3.35	2.25
Pb 4f	1.13	0.29
Cu 2p	8.55	5.63
Zn 2p	0.44	0.62
Sn 3d	–	9.1

samples compared to multicrystalline samples. It is interesting to observe the presence of Sn on the surface of the gridlines, since the silver pastes initially did not have any added Sn or  $\text{SnO}_2$  present (see Table 1). The solder used for the interconnects, however, has a composition of 40% Pb and 60% Sn. It is possible that Sn is corroding and depositing into the surface of Ag busbars and gridlines [32,33].

To further observe what changes occur to the glass layer of the metal contacts close to the busbar where EL dark patterns are seen, we performed high resolution cross-sectional SEM images along almost the full gridline of a control and degraded monocrystalline sample as shown in Fig. 8(a) and (b) respectively. Common among the two is pockets of glass frit, pores among the bulk Ag, and a thin glass layer adjacent to the pyramidal Si surface. All of these are common for such screen-printed metallization. Furthermore, the control sample exhibits a more uniform contrast for the glass layer, while the degraded samples show a broader contrast range. Gaps are noticeable in between the bulk Ag and the glass layer for the degraded sample similar to observations reported by Kraft et al. [15]. Multiple studies have suggested that these signatures (specially the difference in contrast) is due to the degradation of the glass layer [16, 34], possibly because of Pb-elusion/corrosion due to DH exposure. The EDS elemental maps and quantification (see supplementary information S2) also suggests that there is some change in the composition of the glass layer due to DH exposure.

While cross-sectional SEM imaging is a great way to visualize the changes near the glass layer, additional information is need to confirm this observation. Therefore, we removed the bulk Ag to access the underlying glass layer and perform materials characterization. Fig. 9(i) shows the SEM images on the glass layer of control and degraded monocrystalline PERC samples. Although there are no significant visual differences in the images, the EDS mapping and quantification (see supplementary information S3) shows some change in composition along with the presence of Sn on the degraded sample. To verify these observations, high-resolution XPS analysis was performed on the glass layer. Fig. 9(ii) shows the high-resolution Pb 4f XPS spectra. The control sample shows the presence of  $\text{PbO}$ . The degraded sample shows an additional peak of  $\text{Pb}(\text{NO}_3)_2$  along with  $\text{PbO}$ , which could be due to the  $\text{HNO}_3$  etch for bulk Ag removal, forming a surface layer of  $\text{Pb}(\text{NO}_3)_2$ . However, this does not impact the overall content of Pb present in the glass layer. Quantification of the XPS survey spectrums shown in Table 3 suggests that the composition of glass layer is changing after DH exposure. There is less Pb content present in the degraded sample, which is a sign of Pb elusion as mentioned in previous studies [15]. Furthermore, the presence of Sn is confirmed on the glass layer of the degraded sample both in oxidized ( $\text{SnO}_2$ ) and metallic (Sn) form as shown in high-resolution Sn 3d XPS spectra in Fig. 9(iii). Previous reports have talked about Sn transport in the bulk Ag and near the metal-Si interface [35]. Our results confirm the transport of Sn to the glass layer for this mode of degradation.

Darkening of the cell starting from the edge due to DH exposure, which spreads throughout the cell, has been studied previously [11,15]. Since both the modules have clear EVA on the front side, it is natural that

the generation of acetic acid due to EVA hydrolysis is playing a key role in the degradation of both the modules [15]. There is, however, a difference in the backside encapsulation (white vs clear EVA) for the modules. In a recent study, it has been shown that the performance degradation is the worst for modules with white EVA when exposed to DH [36]. Interestingly, although the monocrystalline PERC modules have white EVA in the back, they still show less performance degradation than the multicrystalline Al-BSF modules with clear EVA on the backside. This confirms that the effect of backside EVA is minor in this study, specially for the degradation of the front contacts. Recent DH studies have frequently observed the mode of degradation (EL darkening) starting from the busbar. Many researchers suggested that this pattern is due to the use of Ag pastes that are resistant to acetic acid. Modules using these pastes are usually more tolerant to acetic acid resulting in less performance losses, but show this unique busbar darkening pattern [34,37,38]. This is relatable to our monocrystalline module that shows less performance loss than the multicrystalline module. A recent study by Ino et al. observed similar darkening pattern starting from the busbar and suggested that this is a result of Sn migration, since the same pattern is exhibited on cells with both Pb and Pb-free solder [39]. They also showed that the pattern appears only on the parts of the interconnection ribbon that have been soldered using Pb and Pb-free solder. This strongly suggests that the solder plays a critical role in this mode of contact degradation.

It is possible that the presence of Sn on the gridline surface of the degraded regions is playing a key role in this darkening pattern. We think that Sn, which is a corrosion product of the interconnect, is being carried and deposited on the surface of the nearby silver gridlines. XPS imaging of Sn 3d in Fig. 7(iv) shows how the detected Sn is dispersed along the degraded Ag gridline, which is a sign of Sn being migrated from the interconnects to the nearby region. Moreover, Sn was also found on the glass layer as shown in Fig. 9(iii), suggesting that Sn is transported around or through the bulk Ag into the glass layer. The deposition of the thin layer of Sn could be playing a key role in accelerating the acetic acid corrosion at these locations, mainly within the metal-Si interface. A recent study by Ino et al. reports similar observations and they talk about the mechanism behind this kind of degradation [34]. They proposed a cathodic galvanic corrosion reaction near the interfacial glass layer, due to coating of the Ag metal fingers with corrosion products. This corrosion is initiated due to moisture ingress. When Sn or Pb (base metals) in the solder comes in contact with Ag (noble metal) in the presence of electrolyte, there is an electrode potential difference. This results in a galvanic corrosion. In the next step,  $\text{Sn}^{2+}$  and  $\text{Pb}^{2+}$  are generated by the anodic reaction which are then consumed and deposited as corrosion products by the cathodic reaction on the surface of the nearby Ag finger. These corrosion products deposited on finger surface near the busbar prevents the galvanic reaction and therefore, it than continues further away from the busbar on bare Ag surfaces. At these covered finger areas, some of the electrons now will be consumed by reaction at the interfacial glass layer. There is a similar reaction of consumption of  $\text{Pb}^{2+}$  by the formation of corrosion products, in addition to the Pb elusion proposed by Kraft et al. [15]. As the eluted  $\text{Pb}^{2+}$  ions released from lead acetate and dissolved in water are consumed as corrosion products, the concentration of  $\text{Pb}^{2+}$  ions in solution decreases. Therefore, this will essentially accelerate the Pb elusion reaction and in turns the degradation of the glass layer. A detailed explanation of this mechanism can be found in Ref. [34].

According to the aforementioned mechanism, when the galvanic corrosion product covers the surface of the Ag finger and the number of electrons contributing to the dissolution reaction of the glass layer increases, the glass layer preferentially dissolves under these finger regions covered by corrosion products, resulting in the occurrence of degradation patterns from the busbar. The degraded glass layer causes loss of electrical connection in these regions and in turns increase the series resistance. For silver pastes that are easily corroded by acetic acid, corrosion occurs before Sn covers the Ag finger, and the darkening from

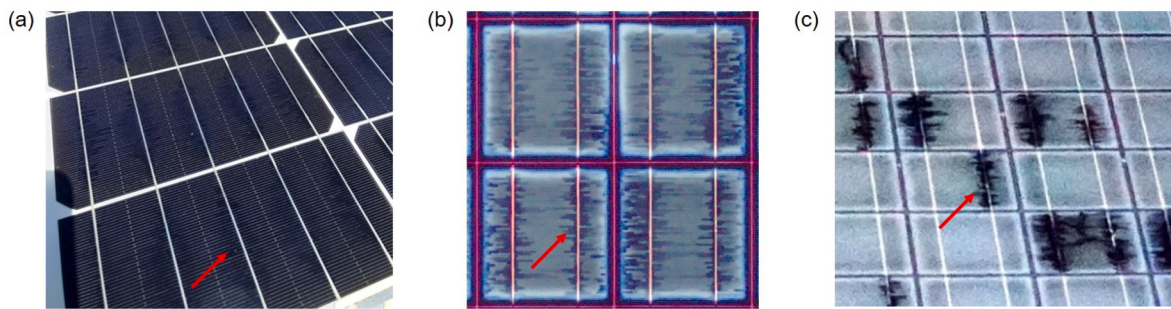


**Fig. 10.** (a) Image of the monocrystalline PERC module after 3200 h of DH. (b) UVF image showing similar patterns from the busbar for field-exposed modules (this image was provided by Will Hobbs at Southern Company) [44]. (c) UVF image showing patterns from the busbar for outdoor installed modules (this image was provided by Andrew Gabor at BrightSpot Automation) [45].

edge moving inwards takes place which has been observed in early DH studies. If the paste is resistant to acetic acid, corrosion of the glass layer starts under the Ag finger covered by the Sn and Pb corrosion products (before corrosion by acetic acid), and darkening patterns starting from the busbar is seen [34]. Our study provides evidence of Sn transport (to the finger surface and interfacial glass layer) and the elusion and re-deposition of Pb on the finger surface, which further confirms this mode of degradation. It also appears that Sn has a greater impact on the contact degradation since even Pb-free solders show the same EL patterns on monocrystalline Al-BSF samples [39]. Also, the same darkening patterns in the EL appear in the monocrystalline PERC samples in this work as in monocrystalline Al-BSF samples in Ref. [39]. Another study by Cumas et al. showed that the darkening pattern from the busbar appears both on multicrystalline and monocrystalline modules [40]. All these examples further reveal that the cell technology is not a contributing factor.

### 3.3. Field relevance

For damp-heat testing, it is strongly suggested that going beyond 1000 h is unnecessary, as it induces conditions that are not seen in the field [37,41–43]. One study showed that water concentration in front of cells after 1000 h of DH is comparable to the calculated water uptake after several years in a tropical climate [42]. Another study showed that in Thailand, a location with exceptionally high humidity, the temperature and humidity conditions induced by DH testing were never seen [41]. They later correlated DH testing hours to years of field exposure and their results suggest that even 1000 h may be excessive. Due to the high amount of humidity introduced during the test, the modules might be susceptible to unique failures or overly severe forms of moisture ingress. Factors such as discoloration, corrosion, and degradation of the polymeric and metallic compounds may be exaggerated. Furthermore, temperature and ambient humidity fluctuations allow moisture to release through the backsheet, whereas DH testing only pushes moisture in.

However, there are cases where the degradation from DH is actually seen on fielded modules. Fig. 10(a) shows an image of the monocrystalline module from this study after 3200 h of DH. The areas where darkening patterns were seen in the EL images actually shows a change in contrast when visually inspected. This suggests that there could be encapsulant delamination in these regions, and could be related to the metallization corrosion pattern. Similar kind of patterns were observed by Gilleland et al. [44] (Fig. 10(b)) after performing UV fluorescence (UVF) imaging on field-exposed modules. Gabor et al., in a recent study also observed similar patterns (Fig. 10(c)) after performing UVF imaging on outdoor installed modules and suggested this could be related to metallization corrosion [45]. These findings suggest that this mode of degradation is highly relevant to the field and not only limited to accelerated DH exposure.

## 4. Conclusion

In this study, we perform a detailed study of the long-term performance and reliability of monocrystalline and multicrystalline PV modules that underwent DH exposure. The primary failure mode induced by DH exposure is resistive, as positively shown via *I*-*V* and EL data. EQE, reflectance, and PL reveal that while recombination degradation occurs, its contribution to module degradation is substantially minor compared to that of resistive losses. Reflectance data show optical losses are insignificant, but the slight reduction in reflectance is likely due to a change in the reflectivity of the gridlines themselves after corrosion. SEM, EDS and XPS analyses on cored samples reveal degradation of the glass layer/metal-Si interface and Sn migration from the interconnections onto the surface of Ag contacts. The deposition of Sn and Pb on the surface of the Ag gridlines play a key role in accelerating the corrosion of the metal-Si interface, which eventually results in loss of electrical connection and EL darkening. Furthermore, we have confirmed that there is transport of Sn to the glass layer due to DH exposure. Since the encapsulant for both modules was EVA, it is obvious that the formation of acetic acid has contributed to PbO dissolution and gap formation. Although Pb played a significant role in contact degradation, Sn migration is the predominant factor.

Our work contributes to the growing amount of evidence that the metal paste and solder composition primarily contributes to DH induced degradation. The paste composition is different based on factors such as wafer crystallinity to promote better contact formation, doping level of layer to be contacted, and on the paste supplier, but these are not the primary factors in DH induced degradation. A potential improvement in PV technology, based on analyzing DH degradation, is to use Pb and Sn free solder; however, this has been known to cause some issues. Another solution is to use an alternative encapsulant material to EVA, which is one of the root causes of metallization corrosion. More research and development could find solutions to push PV towards a metal paste and solder compositions with even greater reliability than it already possesses.

## Declaration of competing interest

The authors declare that they have no known competing financial interests or personal relationships that could have appeared to influence the work reported in this paper.

## Acknowledgment

This work is supported by the U.S. Department of Energy's Office of Energy Efficiency and Renewable Energy (EERE) under Solar Energy Technologies Office (SETO) Agreement Number: DE-EE-0008172. Authors also acknowledge the NSF MRI: ECCS: 1726636 and MCF-AMPAC facility, MSE and CECS. The authors would like to thank Will Hobbs of Southern Company and Andrew Gabor of BrightSpot Automation for

UVF images of PV modules from the field showing potential signs of front contact corrosion. The authors would also like to thank Thomas Shaw and Titel Jurca from the Department of Chemistry, University of Central Florida, for helping with the bulk Ag etching experiment.

## Appendix A. Supplementary data

Supplementary data to this article can be found online at <https://doi.org/10.1016/j.solmat.2021.111468>.

## References

- [1] D.C. Jordan, B. Marion, C. Deline, T. Barnes, M. Bolinger, Pv field reliability status—an analysis of 100 000 solar systems, *Prog. Photovoltaics Res. Appl.* 28 (2020) 739–754, <https://doi.org/10.1002/pip.3262>.
- [2] G.M. Wilson, M.M. Al-Jassim, W.K. Metzger, S.W. Glunz, P. Verlinden, X. Gang, L. M. Mansfield, B.J. Stanberry, K. Zhu, Y. Yan, J.J. Berry, A.J. Ptak, F. Dimroth, B. M. Kayes, A.C. Tamboli, R. Peibst, K.R. Catchpole, M. Reese, C. Klinga, P. Denholm, M. Morjaria, M.G. Deceglie, J.M. Freeman, M.A. Mikofski, D.C. Jordan, G. Tamizhmani, D.B. Sulas, The 2020 photovoltaic technologies roadmap, *J. Phys. Appl. Phys.* (2020), <https://doi.org/10.1088/1361-6463/ab9c6a>.
- [3] D.C. Jordan, S.R. Kurtz, Photovoltaic degradation rates—an analytical review, *Prog. Photovoltaics Res. Appl.* 21 (2013) 12–29, <https://doi.org/10.1002/pip.1182>.
- [4] D.C. Jordan, B. Sekulic, B. Marion, S.R. Kurtz, Performance and aging of a 20-year-old silicon pv system, *IEEE J. Photovoltaics* 5 (2015) 744–751, <https://doi.org/10.1109/JPHOTOV.2015.2396360>.
- [5] R. Jones-Albertus, D. Feldman, R. Fu, K. Horowitz, M. Woodhouse, Technology advances needed for photovoltaics to achieve widespread grid price parity, *Prog. Photovoltaics Res. Appl.* 24 (2016) 1272–1283, <https://doi.org/10.1002/pip.2755>.
- [6] H. Seigneur, N. Mohajeri, R.P. Brooker, K.O. Davis, E.J. Schneller, N.G. Dhere, M. P. Rodgers, J. Wohlgemuth, N.S. Shiradkar, G. Scardera, et al., Manufacturing metrology for c-si photovoltaic module reliability and durability, part i: feedstock, crystallization and wafering, *Renew. Sustain. Energy Rev.* 59 (2016) 84–106.
- [7] K.O. Davis, M.P. Rodgers, G. Scardera, R.P. Brooker, H. Seigneur, N. Mohajeri, N. G. Dhere, J. Wohlgemuth, E. Schneller, N. Shiradkar, G. Scardera, et al., Manufacturing metrology for c-si module reliability and durability part ii: cell manufacturing, *Renew. Sustain. Energy Rev.* 59 (2016) 225–252.
- [8] E.J. Schneller, R.P. Brooker, N.S. Shiradkar, M.P. Rodgers, N.G. Dhere, K.O. Davis, H.P. Seigneur, N. Mohajeri, J. Wohlgemuth, G. Scardera, et al., Manufacturing metrology for c-si module reliability and durability part iii: module manufacturing, *Renew. Sustain. Energy Rev.* 59 (2016) 992–1016.
- [9] Z. Liu, M.L. Castillo, A. Youssef, J.G. Serdy, A. Watts, C. Schmid, S. Kurtz, I. M. Peters, T. Buonassisi, Quantitative analysis of degradation mechanisms in 30-year-old pv modules, *Sol. Energy Mater. Sol. Cell.* 200 (2019) 110019, <https://doi.org/10.1016/j.solmat.2019.110019>.
- [10] A. Omazic, G. Oreski, M. Halwachs, G. Eder, C. Hirschl, L. Neumaier, G. Pinter, M. Erceg, Relation between degradation of polymeric components in crystalline silicon PV module and climatic conditions: a literature review, *Sol. Energy Mater. Sol. Cell.* 192 (2019) 123–133, <https://doi.org/10.1016/j.solmat.2018.12.027>.
- [11] C. Peike, S. Hoffmann, P. Hülsmann, B. Thaidigsmann, K. Weiß, M. Koehl, P. Bentz, Origin of damp-heat induced cell degradation, *Sol. Energy Mater. Sol. Cell.* 116 (2013) 49–54.
- [12] J. Zhu, M. Koehl, S. Hoffmann, K.A. Berger, S. Zamini, I. Bennett, E. Gerritsen, P. Malbranche, P. Pugliatti, A. Di Stefano, F. Aleo, D. Bertani, F. Paletta, F. Roca, G. Gradić, M. Pellegrino, O. Zubillaga, F.J.C. Iranzo, A. Pozza, T. Sample, R. Gottschalg, Changes of solar cell parameters during damp-heat exposure, *Prog. Photovoltaics Res. Appl.* 24 (2016) 1346–1358, <https://doi.org/10.1002/pip.2793>.
- [13] A.W. Czanderna, F.J. Pern, Encapsulation of PV modules using ethylene vinyl acetate copolymer as a pottant: a critical review, *Sol. Energy Mater. Sol. Cell.* 43 (1996) 101–181, [https://doi.org/10.1016/0927-0248\(95\)00150-6](https://doi.org/10.1016/0927-0248(95)00150-6).
- [14] M.D. Kempe, G.J. Jorgensen, K.M. Terwilliger, T.J. McMahon, C.E. Kennedy, T. T. Borek, Acetic acid production and glass transition concerns with ethylene-vinyl acetate used in photovoltaic devices, *Sol. Energy Mater. Sol. Cell.* 91 (2007) 315–329.
- [15] A. Kraft, L. Labusch, T. Ensslen, I. Dürr, J. Bartsch, M. Glatthaar, S. Glunz, H. Reinecke, Investigation of acetic acid corrosion impact on printed solar cell contacts, *IEEE J. Photovoltaics* 5 (2015) 736–743.
- [16] T. Semba, Corrosion mechanism analysis of the front-side metallization of a crystalline silicon PV module by a high-temperature and high-humidity test, *Jpn. J. Appl. Phys.* 59 (2020), 054001, <https://doi.org/10.35848/1347-4065/ab8274>.
- [17] IEC 61215-2: 2016, Terrestrial Photovoltaic (Pv) Modules-Design Qualification and Type Approval-Part 2: Test Procedures, International Electrotechnical Commission, 2016.
- [18] X. Ma, W.-H. Huang, E. Schnabel, M. Köhl, J. Brynjarsdóttir, J. Braid, R. French, Data-driven i-v feature extraction for photovoltaic modules, *IEEE J. Photovoltaics* (2019) 1–8, <https://doi.org/10.1109/JPHOTOV.2019.2928477>.
- [19] H. Moutinho, S. Johnston, B. To, C.-S. Jiang, C. Xiao, P. Hacke, J. Moseley, J. Tynan, N. Dhere, M. Al-Jassim, Development of coring procedures applied to Si, CdTe, and CIGS solar panels, *Sol. Energy* 161 (2018) 235–241, <https://doi.org/10.1016/j.solener.2017.11.071>.
- [20] H. Moutinho, B. To, D.B. Sulas-Kern, C.-S. Jiang, M. Al-Jassim, S. Johnston, Advances in coring procedures of silicon photovoltaic modules, in: 2019 IEEE 46th Photovoltaic Specialists Conference (PVSC), IEEE, Chicago, IL, USA, 2019, pp. 2008–2012, <https://doi.org/10.1109/PVSC40753.2019.8980840>.
- [21] E.J. Schneller, K. Öğütman, S. Guo, W.V. Schoenfeld, K.O. Davis, Crystalline silicon device loss analysis through spatially resolved quantum efficiency measurements, *IEEE J. Photovoltaics* 7 (2017) 957–965.
- [22] M.J. Hossain, E.J. Schneller, M. Li, K.O. Davis, Incorporation of spatially-resolved current density measurements with photoluminescence for advanced parameter imaging of solar cells, *Sol. Energy Mater. Sol. Cell.* 199 (2019) 136–143.
- [23] M.J. Hossain, G. Gregory, E.J. Schneller, A.M. Gabor, A.L. Blum, Z. Yang, D. Sulas, S. Johnston, K.O. Davis, A comprehensive methodology to evaluate losses and process variations in silicon solar cell manufacturing, *IEEE J. Photovoltaics* 9 (2019) 1350–1359.
- [24] N. Iqbal, M. Li, G. Gregory, S. Dahal, S. Bowden, K.O. Davis, Recombination and resistive losses of transferred foil contacts for silicon heterojunction solar cells, *Phys. Status Solidi Rapid Res. Lett.* 14 (2020) 2000368, <https://doi.org/10.1002/pssr.202000368>.
- [25] P. Ferrada, D. Rudolph, C. Portillo, A. Adrian, J. Correa-Puerta, R. Sierpe, V. del Campo, M. Flores, T.P. Corrales, R. Henríquez, et al., Interface analysis of ag/n-type si contacts in n-type pert solar cells, *Prog. Photovoltaics Res. Appl.* 28 (2020) 358–371.
- [26] M. Li, N. Iqbal, Z. Yang, X. Lin, N.K. Pannaci, C. Avalos, T. Shaw, K. Davis, et al., A comprehensive evaluation of contact recombination and contact resistivity losses in industrial silicon solar cells, *IEEE J. Photovoltaics* 10 (2020) 1277–1282.
- [27] R. Sinton, A. Cuevas, A Quasi-steady-state open-circuit voltage method for solar cell characterization, in: 16th European Photovoltaic Solar Energy Conference, Glasgow, Scotland, 2000, pp. 1152–1155.
- [28] C.A. Castro, P. Osorio, A. Sienkiewicz, C. Pulgarin, A. Centeno, S.A. Giraldo, Photocatalytic production of lo2 and oh mediated by silver oxidation during the photoactivation of escherichia coli with tio2, *J. Hazard Mater.* 211 (2012) 172–181, <https://doi.org/10.1016/j.jhazmat.2011.08.076>.
- [29] A.M. Ferraria, A.P. Carapeto, A.M.B. do Rego, X-ray photoelectron spectroscopy: silver salts revisited, *Vacuum* 86 (2012) 1988–1991, <https://doi.org/10.1016/j.vacuum.2012.05.031>.
- [30] W. Oh, S. Kim, S. Bae, N. Park, Y. Kang, H.-S. Lee, D. Kim, The degradation of multi-crystalline silicon solar cells after damp heat tests, *Microelectron. Reliab.* 54 (2014) 2176–2179, <https://doi.org/10.1016/j.micrel.2014.07.071>.
- [31] D. Kiliani, A. Herguth, G. Hahn, V. Rutka, M. Junk, Fitting of lateral resistances in silicon solar cells to electroluminescence images, in: 24th European Photovoltaic Solar Energy Conference, 2009, pp. 2088–2090.
- [32] P. Schmitt, P. Kaiser, C. Savio, M. Tranzit, U. Eitner, Intermetallic phase growth and reliability of sn-ag-soldered solar cell joints, *Energy Procedia* 27 (2012) 664–669, <https://doi.org/10.1016/j.egypro.2012.07.126>.
- [33] T. Geipel, M. Moeller, J. Walter, A. Kraft, U. Eitner, Intermetallic compounds in solar cell interconnections: microstructure and growth kinetics, *Sol. Energy Mater. Sol. Cell.* 159 (2017) 370–388, <https://doi.org/10.1016/j.solmat.2016.08.039>.
- [34] Y. Ino, S. Asao, K. Shirasawa, H. Takato, Investigation of degradation mode spreading interconnectors by pressure-cooker testing of photovoltaic cells, *IEEE J. Photovoltaics* 10 (2019) 188–196.
- [35] T. Semba, T. Shimada, T. Fujita, Influence of front-side ag metallization on high temperature and high humidity test of crystalline silicon pv module, in: 2019 IEEE 46th Photovoltaic Specialists Conference (PVSC), 2019, pp. 1525–1528.
- [36] A. Curran, M. Wang, C. Whitaker, T. Moran, B. Huey, J. Dai, J.-N. Jaubert, D. J. Colvin, N. Iqbal, K.O. Davis, et al., Degradation of bifacial perc and al-bsf cell minimodules with white and clear encapsulant combinations in modified damp heat, in: 2020 47th IEEE Photovoltaic Specialists Conference (PVSC), IEEE, 2020, pp. 2076–2082.
- [37] T.J. Trout, W. Gambogi, T. Felder, K.R. Choudhury, L. Garreau-Iles, Y. Heta, K. Stika, Pv module durability -connecting field results, accelerated testing, and materials, in: 2017 IEEE 44th Photovoltaic Specialist Conference (PVSC), 2017, pp. 2312–2317.
- [38] A. Masuda, Y. Hara, Guiding principle for crystalline si photovoltaic modules with high tolerance to acetic acid, *Jpn. J. Appl. Phys.* 57 (2018), 04FS06.
- [39] Y. Ino, S. Asao, K. Shirasawa, H. Takato, Effect of soldering on the module degradation along bus bar in dh test and pct for crystalline si pv modules, in: 2018 IEEE 7th World Conference on Photovoltaic Energy Conversion (WCPEC) (A Joint Conference of 45th IEEE PVSC, 28th PVSEC 34th EU PVSEC), 2018, pp. 3552–3557.
- [40] C. Camus, A. Adegbienro, J. Ermer, V. Suryaprakash, J. Hauch, C.J. Brabec, Influence of pre-existing damages on the degradation behavior of crystalline silicon photovoltaic modules, *J. Renew. Sustain. Energy* 10 (2018), 021004.
- [41] J.H. Wohlgemuth, M.D. Kempe, Equating damp heat testing with field failures of PV modules, in: 2013 IEEE 39th Photovoltaic Specialists Conference (PVSC), IEEE, Tampa, FL, USA, 2013, pp. 126–131, <https://doi.org/10.1109/PVSC.2013.6744113>.
- [42] P. Hülsmann, K.-A. Weiss, Simulation of water ingress into pv-modules: iec-testing versus outdoor exposure, *Sol. Energy* 115 (2015) 347–353, <https://doi.org/10.1016/j.solener.2015.03.007>.

- [43] M. Koehl, S. Hoffmann, S. Wiesmeier, Evaluation of damp-heat testing of photovoltaic modules, *Prog. Photovoltaics Res. Appl.* 25 (2017) 175–183, <https://doi.org/10.1002/pip.2842>.
- [44] B. Gilleland, W.B. Hobbs, J.B. Richardson, High throughput detection of cracks and other faults in solar pv modules using a high-power ultraviolet fluorescence imaging system, in: 2019 IEEE 46th Photovoltaic Specialists Conference (PVSC), IEEE, 2019, pp. 2575–2582.
- [45] A.M. Gabor, P. Knolle, Uv fluorescence for defect detection in residential solar panel systems, in: 2021 IEEE 48th Photovoltaic Specialists Conference (PVSC), IEEE, 2021, pp. 2575–2579, <https://doi.org/10.1109/PVSC43889.2021.9518884>.